

Near Infrared (NIR) Strong Field Ionization and Imaging of C₆₀ Sputtered Molecules: Overcoming Matrix Effects and Improving Sensitivity

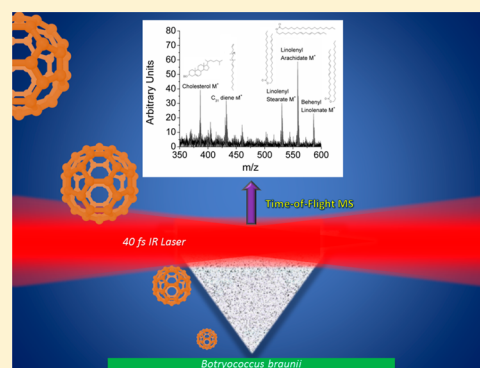
Andrew Kucher,[†] Lauren M. Jackson,[†] Jordan O. Lerach,[†] A. N. Bloom,[†] N. J. Popczun,[†] Andreas Wucher,[‡] and Nicholas Winograd^{*,†}

[†]Chemistry Department, The Pennsylvania State University, 104 Chemistry Building, University Park, Pennsylvania 16802, United States

[‡]Fachbereich Physik, Universitaet Duisburg-Essen, 47048 Duisburg, Germany

Supporting Information

ABSTRACT: Strong field ionization (SFI) was applied for the secondary neutral mass spectrometry (SNMS) of patterned rubrene films, mouse brain sections, and *Botryococcus braunii* algal cell colonies. Molecular ions of rubrene, cholesterol, C₃₁ diene/triene, and three wax monoesters were detected, representing some of the largest organic molecules ever ionized intact by a laser post-ionization experiment. In rubrene, the SFI SNMS molecular ion signal was ~4 times higher than in the corresponding secondary-ion mass spectroscopy (SIMS) analysis. In the biological samples, the achieved signal improvements varied among molecules and sampling locations, with SFI SNMS, in some cases, revealing analytes made completely undetectable by the influence of matrix effects in SIMS.



Recent advances in cluster secondary ion mass spectrometry (SIMS) have opened new applications in molecule-specific imaging, particularly in the biomaterials arena.¹ However, a major problem continues to be sensitivity, since there is a limited number of analyte molecules that lie within a pixel of submicrometer dimensions.² For example, there are on the order of 10⁶ molecules per monolayer in a 1 μm² pixel and, with the secondary ion yield for a typical biomolecule in the range of 10⁻³–10⁻⁸, the ultimate count rate is frequently too small for imaging. Sensitivity can be gained by molecular depth profiling and adding signal from subsurface layers, now a realistic possibility with many cluster ion sources, at the expense of depth resolution and three-dimensional imaging capabilities. Ionization matrix effects are also problematic, particularly for achieving quantitative measurements. Since ionization often occurs via protonation of a neutral molecule to form [M + H]⁺ ions, charge transfer resulting in ion suppression is commonly observed in complex, multicomponent samples such as biological tissue.^{3,4}

To mitigate the manifestation of these issues and to improve the prospects for high spatial resolution molecule-specific imaging, several groups have attempted to ionize the neutral species in the plume of sputtered molecules above the sample using laser-based photoionization techniques.^{5–11} This approach, laser post-ionization (LPI) secondary neutral mass spectrometry (SNMS), has been explored for many years, with mixed levels of success. It has been particularly effective at elemental ionization,^{12,13} while molecules have remained

problematic. The main challenge is the ability to produce efficient ionization without inducing large amounts of photo-fragmentation. Applications of various ionization methods have been reported, including single photon ionization,^{14,15} as well as resonantly enhanced¹⁶ and nonresonant multiphoton ionization.^{17–19} However, these LPI approaches have known limitations. In single photon ionization, many molecular ionization potentials are outside the energy range of readily available VUV laser sources, while in multiphoton ionization excess energy absorption often leads to extensive fragmentation.

Beyond established methods, strong field ionization (SFI), which is an area of ongoing research because of its importance in attosecond spectroscopy,^{20,21} appears to be a promising new post-ionization approach.^{11,22,23} SFI occurs at intensities of >10¹³ W/cm², where the laser field strength becomes comparable to the Coulomb field binding the valence electrons and molecular energy levels are heavily Stark-shifted away from their field-free values.^{24–26} The resulting ionization dynamics can involve field phenomena such as tunneling or barrier suppression ionization, leading to the production of intact molecular ions (adiabatic response), or energy absorption from the laser field and the creation of extensive fragmentation (nonadiabatic response).^{27,28} Molecular structure—and, in

Received: April 4, 2014

Accepted: August 9, 2014

Published: August 9, 2014

particular, the polarizability of the target molecule—is a major consideration in the outcome of SFI, as are the laser intensity and wavelength.^{11,20,27–40} Fundamental gas-phase studies have demonstrated that ultrashort pulses at IR wavelengths and at molecule specific optimized intensities can favor adiabatic dynamics over nonadiabatic dynamics in the visible, producing near fragment free spectra for some analytes.^{27,28,30,31}

Despite success in fundamental experiments, the application of SFI to SNMS presents a unique challenge as sputtered molecules disperse into a plume of increasing size with distance from the sample.⁴¹ The laser focus in SFI must effectively overlap this plume while still generating fields in excess of 10^{13} W/cm². Hence, a powerful laser system capable of delivering tunable IR laser pulses at focal diameters typically on the order of hundreds of micrometers is necessary. These types of systems are now commercially available, and the merits of such a laser for efficient post-ionization of molecules desorbed from a solid surface can be explored. In a recent pilot study using β -estradiol as a model system, we have performed a detailed investigation of the photoionization and fragmentation efficiency of both gas-phase and sputtered molecules, as a function of laser wavelength and intensity.⁴² It was found that the optimum ionization efficiency, along with the least amount of photofragmentation, is achieved at a “saturation intensity” of $\sim 10^{13}$ W/cm², which gradually increases with increasing wavelength. At the highest achievable laser intensity ($\sim 10^{15}$ W/cm²), on the other hand, the molecular ion signal is found to decrease, because of increased photofragmentation. Moreover, this intensity regime is only reached with a tightly focused laser, which samples only a small fraction of the plume of sputtered material. Optimum conditions for efficient post-ionization are therefore established when the laser beam is defocused to such an extent as to maintain the saturation intensity in the ionizing region while, at the same time, sampling a substantially increased fraction of the sputtered plume.

The scope of the present investigation is to detail the application of such a strategy for practical LPI SNMS studies across a range of molecular structures and to biological samples. First, the polycyclic aromatic hydrocarbon rubrene is imaged in a model patterned film, illustrating the general experimental approach. Next, two examples of the first application of SFI in biological analysis are presented, starting with studies of the spatial distribution of cholesterol in mouse brain tissues, and followed by the detection of a range of hydrocarbons in *Botryococcus braunii* (*B. braunii*) algal cell colonies. The results show that the sensitivity of SFI SNMS can exceed that of SIMS, while also minimizing matrix ionization effects. In addition, as a range of molecular structures are successfully post-ionized intact in this study, this suggests that SFI will be more generally amenable to the study of complex systems than previous LPI approaches.

■ EXPERIMENTAL SECTION

The TOF-SIMS instrument employed in these experiments is similar to one described in detail previously.⁴³ Briefly, it consists of a 20 keV C₆₀⁺ primary ion gun (Ionoptika IOG C60-20),⁴⁴ a temperature controllable sample stage, and a reflectron mass spectrometer with a mass resolution of ~ 2000 . A C₆₀⁺ ion pulse of 2000 ns duration and a 1 kHz repetition rate was employed for both the SIMS and LPI SNMS experiments. The relatively long ion pulse was utilized in order to fill the post-ionization volume with sputtered neutral particles of all

emission velocities, thereby maximizing the SNMS detection sensitivity across the entire mass range, as discussed previously.⁴⁵ The beam current was typically 25 pA, with the fluence during all experiments below the static limit ($< 10^{12}$ ions/cm²). Because of the complexity of the multicomponent samples investigated, at this time, it is difficult to estimate the amount of material removed. Details of the ion extraction methods employed are provided in the Supporting Information.

All sputtered analyses were conducted at a sample temperature of 100 K, to avoid any thermal sublimation that might occur, especially from the biological samples. The base pressure of the SIMS instrument was $< 2 \times 10^{-9}$ mbar. It is important to keep this value as low as possible to avoid significant signal contributions from the photoionization of the residual gas.

The laser system employed for LPI SNMS produces tunable 40-fs pulses in the wavelength range of 1160–2580 nm. A more-detailed description of the system is presented in the Supporting Information.

When observed, gain saturation produced by overabundant post-ionized m/z 1–100 ions is corrected by deflecting them away from the multichannel plate detector. Additional details are presented in the Supporting Information.

Descriptions of the sample preparation methods for the patterned rubrene and pure cholesterol films are presented in the Supporting Information. Tissue imaging experiments were performed on cryogenically frozen mouse brains obtained from Rockland Immunochemicals, Inc. They were sliced into 10- μ m-thick sections using a cryostat and mounted onto clean ITO glass. Samples were analyzed in their natural frozen state, without any washing steps to remove native salts.

Race-A *B. braunii* algae was cultured from algal specimen No. 572 (UTEX The Culture Collection of Algae) under conditions described elsewhere.⁴⁶ A 2-mL aliquot of the algal suspension in Modified Bold 3N Medium was centrifuged and the supernatant was discarded. This was followed by drop-drying a 10- μ L aliquot of the algal cells onto precut 5 mm \times 5 mm Si shards in a vacuum desiccator. The deposited cell colonies nearly covered the shard. The samples were not washed to remove salts and were introduced into vacuum without any further processing. The extracellular matrix of the *B. braunii* algae protected the cells within the colony from lysing under vacuum.⁴⁷

■ RESULTS AND DISCUSSION

The low secondary ion formation probabilities of sputtered molecules and their susceptibility to matrix effects have been at the forefront of outstanding challenges in SIMS. In biological applications in particular, these problems are exacerbated by the low analyte concentrations in complex chemical environments. It has always been hoped that SNMS would increase the available signal in these applications, and, indeed, SFI has been shown capable of this for the analytes presented in this work (see Figure S-1 in the Supporting Information and Table 1). The intact post-ionization of fairly large (m/z 380–600) molecules, featuring a variety of chemical structures, with most being primarily σ -bonded, is novel among SNMS approaches, and occurs despite the presence of a degree of nonadiabatic ionization dynamics, visible most clearly in the model imaging studies of rubrene patterned films.

Rubrene Patterned Films. Rubrene is selected as a model compound because (i) it contains both conjugated and nonconjugated parts and (ii) its molecular weight (532.7 Da) falls within the range of many biologically important targets. By

Table 1. Intact Molecular Ions Produced in SFI SNMS and SIMS, with Typical Signal Ratios

name ^a	formula	molar mass (g/mol)	SIMS	SNMS	SNMS/SIMS
rubrene	C ₄₂ H ₂₈	532.7	M ⁺	M ⁺	4.3 ± 0.7
cholesterol	C ₂₇ H ₄₆ O	386.7	M-H ⁺	M ⁺	1-3 ^b
C ₃₁ diene	C ₃₁ H ₆₀	432.8	M+H ⁺	M ⁺	0.6-3 ^b
C ₃₁ triene	C ₃₁ H ₅₈	430.8	M ⁺	M ⁺	0.6-3 ^b
linolenyl stearate*	C ₃₆ H ₆₆ O ₂	530.9	M ⁺	M ⁺	1-2 ^b
linolenyl arachidate*	C ₃₈ H ₇₀ O ₂	559.0	M ⁺	M ⁺	1-2 ^b
behenyl linolenate*	C ₄₀ H ₇₄ O ₂	587.0	M ⁺	M ⁺	1-2 ^b

^aAsterisk symbol (*) denotes a likely isomer. ^bTypically observed SFI SNMS signal improvements over SIMS in the biological applications discussed. However, at some sampling locations, the SIMS signal was nonexistent, because of severe matrix effects. In these cases, only SFI SNMS produced a viable spectrum.

observing the extent of photodissociation in SFI SNMS spectra, the prospects for and challenges to the post-ionization of larger and less-stable molecules can be assessed.

In determining the extent of nonadiabatic dynamics in rubrene, it is important to separate the intact post-ionization of an emitted molecule or fragment on one hand, from laser-induced photodissociation accompanying the photoionization processes on the other. In doing so, higher mass fragments have more utility, as the lower mass ions are more likely to have substantial contributions from the latter process. Moreover,

most sputtered low-mass fragments have been predicted to originate from the area directly below the primary ion impact point, unlike intact molecules, which are ejected from the periphery of the formed crater.⁴⁸ Their sputtering dynamics result in much higher internal energies than those of intact molecules, and as a result their photodissociation thresholds may be much lower.

In Figure 1, the SFI SNMS and SIMS spectra of rubrene are presented. The high-mass region of both spectra (Figure 1c) is fairly similar, implying that they are both indicative of the same sputtering dynamics. Deviations start to appear at $m/z \sim 376$, where a major high-mass fragment forms via the loss of two benzene rings σ -bonded to the main structure. Relative to the molecular ion, this peak is more than twice as large in the SFI SNMS, compared to the SIMS spectrum. This implies that the SFI process in rubrene induces additional fragmentation of the intact neutral molecule, beyond that created by the primary ion beam, because of nonadiabatic ionization dynamics in some of the sputtered molecules.

In general, the amount of fragmentation in the SFI SNMS spectra of rubrene greatly exceeds what is observed in SIMS. This is a situation that is similar to our analysis of β -estradiol, where we determined that C₆₀⁺ sputtering imparts ~ 1 eV of internal energy to intact β -estradiol molecules.⁴² The excess energy influences the photoionization process, shifting the mechanism to lower intensity (associated with a lower saturation intensity (I_{sat})), compared to the gas-phase molecule. Moreover, it also likely lowers the threshold for molecular photofragmentation. In addition, sputtered neutral fragments possess much higher internal energies than the molecular ion,⁴⁸

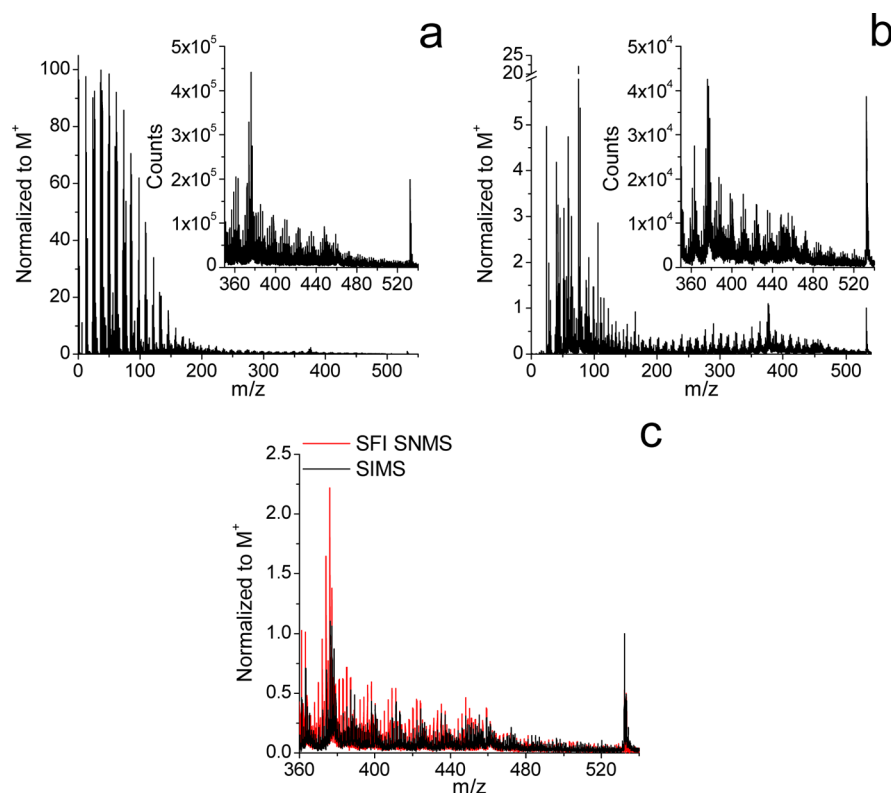


Figure 1. Comparison of the relative amounts of fragmentation in the SFI SNMS and SIMS spectra of a patterned rubrene film. The spectra are normalized to the molecular ion signal, while the insets show direct experimental signal: (a) SFI SNMS using 1350 nm, 2×10^{13} W/cm²; (b) SIMS, the large peak at m/z 75 is not associated with rubrene, it is the signal of a residual salt from a developer solution used in the patterning process. (c) Overlay of the two high-mass regions in the inset of panels a and b, normalized to their respective molecular ion signal.

and very likely undergo further photofragmentation. Overall, the internal energy induced by sputtering is likely the major cause of the large difference in the observed fragment levels in SNMS and SIMS spectra.

The large fragment signal levels observed in this model rubrene film are indicative of the challenges of extending SFI SNMS to complex biological samples where analytes in the lower mass ranges are of interest. In such samples all organic molecules will contribute to the nonspecific low mass hydrocarbon fragment signals, likely producing ion intensities orders of magnitude greater than those of any ions of interest in this mass range. High-resolution mass spectrometers will be necessary to address this problem in such analyses.

Despite the challenges posed by fragments in the lower mass range, post-ionization by SFI in rubrene is encouraging. Although previous gas-phase studies of molecules with extensive delocalized π -bonding had revealed an increasing tendency toward nonadiabatic dynamics with increasing molecular size,^{31,36} the effect observed here is not severe enough to limit the utility of SFI SNMS. The post-ionized molecular ion signal of rubrene is 4.3 ± 0.7 times higher than its secondary-ion counterpart (see insets in Figures 1a and 1b), and enables a commensurate increase in the imaging quality of the patterned film, as shown in Figure 2.

Considering the under-sampling of the sputtered plume in the post-ionization experiment ($\sim 25\%$ is sampled; see the Supporting Information for laser system details), the maximum achievable SFI SNMS signal enhancement for rubrene should

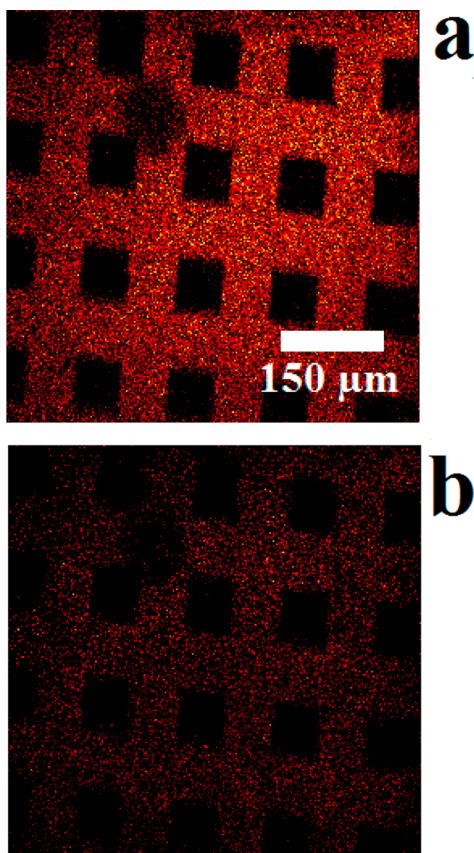


Figure 2. Comparison of the (a) SFI SNMS using 1350 nm, 2×10^{13} W/cm², and (b) SIMS chemical imaging of a patterned rubrene film. The molecular ion is mapped, detected in each analysis under identical sputtering conditions.

be on the order of 20. This number is interesting since it provides an upper limit for the secondary ion formation probability of the molecular ions (reflected by the ratio of the SIMS and SNMS signal levels). Assuming 100% post-ionization efficiency, the data imply that $<5\%$ of sputtered intact rubrene molecules end up as secondary ions. Since the actual intact post-ionization efficiency is smaller due to photofragmentation, this number is an upper bound.

Mouse Brain Tissue Imaging. With our experimental protocols established, and with the knowledge that SFI yields high-intensity molecular-ion signals for sterols,⁴² we next show the feasibility of using it to map the spatial distribution of cholesterol directly in rat brain tissue. Cholesterol plays numerous important neurological functions, among them being involved in myelin formation and synaptogenesis.⁴⁹

It is of note that the characteristic high mass signals of cholesterol are very different in SIMS and SFI SNMS spectra (see Figure 3). The $M-OH^+$ fragment is of a higher intensity in

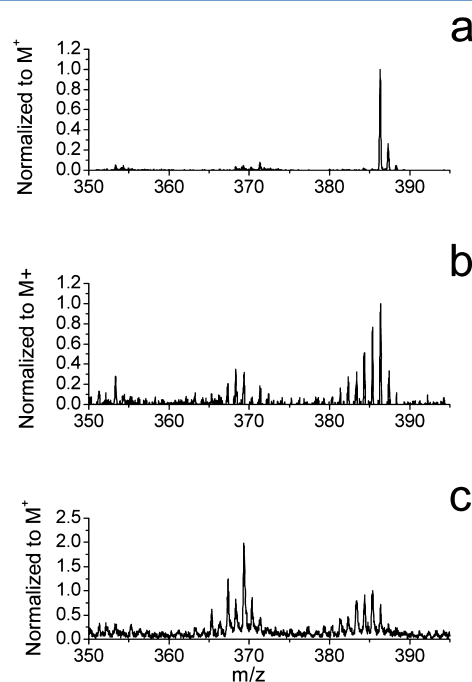


Figure 3. High mass spectral region of gas-phase- and physical-vapor-deposited cholesterol films: (a) gas phase ionization by 1750 nm, 5×10^{13} W/cm²; (b) SFI SNMS of a vapor-deposited film using 1700 nm, 5×10^{13} W/cm²; and (c) SIMS spectrum of a vapor-deposited film. The high-mass regions are presented exclusively, because detector gain saturation in the SFI SNMS spectrum prevented an accurate measurement of the low-mass portion.

SIMS spectra than the $M-H^+$ pseudo-molecular ion. However, this is not case in post-ionization, indicating that it is purely due to the secondary ion formation probability, rather than actual sputtering dynamics.

In Figure 4, the analyses of two mouse brain sections are presented. Two different wavelengths were used for SNMS, showing that a range of wavelengths can produce intact cholesterol ions, and the ionization processes is not a resonance effect. Comparison of the SFI SNMS and corresponding SIMS spectra highlights the sensitivity of SIMS to matrix effects such as ion suppression. In Sample 1 (see Figures 4a and 4b), both spectra show analogous information, regarding the presence of cholesterol. Conversely, in Sample 2 (see Figures 4c and 4d),

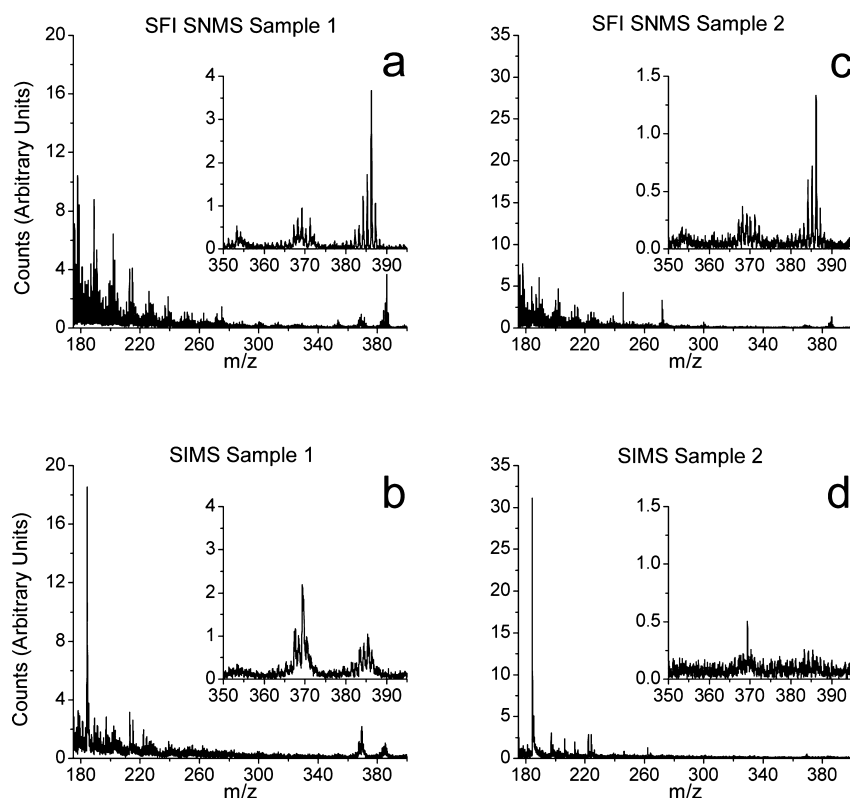


Figure 4. Mouse brain tissue spectra: (a) Sample 1, SFI SNMS using 1700 nm, 6×10^{13} W/cm²; (b) Sample 1, SIMS; (c) Sample 2, SFI SNMS using 1350 nm, 3×10^{13} W/cm²; and (d) Sample 2, SIMS.

the SFI SNMS and SIMS analyses show distinct variations. The secondary ion spectrum is dominated by the lipid phosphatidylcholine (PC) headgroup fragment (m/z 184), while its cholesterol molecular-ion signal is close to the noise threshold. However, the SFI SNMS spectrum reveals that abundant cholesterol is indeed present in the sampled area but is being suppressed during SIMS. Similar phenomena were observed in two-component model Langmuir–Blodgett films of cholesterol and POPC/sphingomyelin.⁵⁰ There it was shown that proton transfer assists lipid ionization⁵¹ and causes suppression of the cholesterol secondary ion. In the present mouse brain tissue analysis, SFI SNMS reveals that there is a likely co-localization of lipids and cholesterol in Sample 2 that is masked by ion suppression in SIMS. Although Figure 4 presents spectra from two different brain sections, matrix effects analogous to those occurring in Sample 2 were also observed in Sample 1, depending on the probed area.

An unfortunate side effect of the greater fragmentation observed in the SFI SNMS spectra is the overlap of the PC headgroup signal by more-abundant cholesterol fragments, making it unavailable for chemical mapping, unlike the strong signal available in SIMS. This observation is consistent with the notion that this species has an extraordinarily high secondary-ion formation probability. In addition, the higher internal energy of the PC headgroup, itself a product of primary-ion-beam-induced fragmentation, may lower the threshold to its further photodissociation in LPI. In any case, these data highlight the advantages of combining insights from both SFI SNMS and SIMS, to provide a more complete surface analysis than available independently.

The SIMS images (Figures 5a–c) and analogous SFI SNMS images (Figures 5d–f) of the cholesterol molecular ion (M^+ –

xH , $x = 0–4$) distributions in several brain sections are shown in Figure 5. The post-ionization signal improvements vary somewhat, depending on the sampled location, with the SFI SNMS versus SIMS integrated count ratios varying between 1 and 3. Using the same arguments as those with rubrene, regarding the limited post-ionization efficiency, because of the under-sampling of the plume, one finds that the secondary-ion formation probability of sputtered cholesterol molecules cannot be greater than $\sim 8\%$.

***B. braunii* Algal Cell Colonies.** As observed in the mouse brain tissue analyses, SFI SNMS decouples ionization from the effects of the local chemical environment. This enables analysis not only free of ion suppression, but also unaffected by native salts. In contrast, the normal application of SIMS in bioanalysis often requires that sample preparation methods include numerous washing steps to remove them. Otherwise, often severe matrix effects may influence the secondary-ion signal. However, sample washes may not always be ideal, as questions can be raised about changes to native distributions and concentrations of analytes. SFI SNMS makes direct analysis possible in *B. braunii*, since it is more amenable to the intact post-ionization of its extensively σ -bonded molecules than other LPI methods.

B. braunii is a green microalga that produces a considerable amount of hydrocarbons and is being investigated as a possible biofuel candidate.^{52–56} Its colonies possess the unusual property of being encased in a lipid envelope,⁵⁷ with the three major races of *B. braunii* differentiated by the type of hydrocarbons they generate and excrete into the extracellular matrix. A forthcoming publication will present an in-depth SIMS study of *B. braunii*,⁴⁶ while the focus of the present investigation is to illustrate the expansion of SFI SNMS

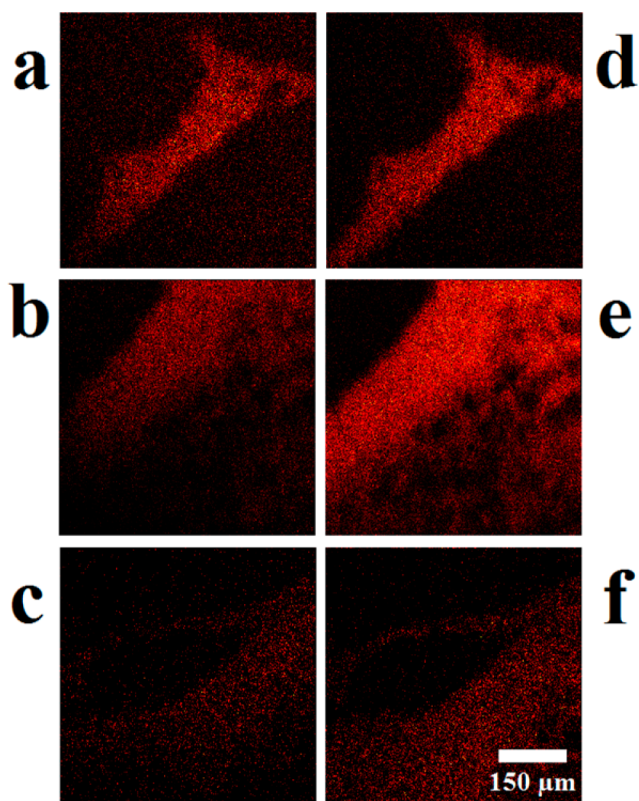


Figure 5. Cholesterol $M^+ - xH$ ($x = 0-4$) distribution in mouse brain tissue slices: (a–c) SIMS images and (d–f) corresponding SFI SNMS images. In panels d and e, SFI SNMS employed 1350 nm, 2.8×10^{13} W/cm² and the molecular ion signal was equal to and three times higher than that in the corresponding SIMS image, whereas in panel f, 1700 nm, 6×10^{13} W/cm² was used, with the SFI SNMS signal being double the corresponding SIMS signal. The variable degrees of improvement were primarily the result of matrix effects influencing the secondary ions. Note that both wavelengths produce a good molecular ion signal in SFI SNMS, suggesting a lack of strong wavelength dependence during the photoionization process.

capabilities to include the analysis of complex biological samples. In these algal colonies, SFI SNMS has enabled the intact post-ionization of cholesterol, C₃₁ diene/triene, and wax monoester molecules from a direct sampling of a *B. braunii* race A culture without pretreatment to remove salts, both residual from the growth media and native to the cells.

Inconsistencies between SFI SNMS and SIMS spectra in Figure 6 reveal that the secondary ions from *B. braunii* are strongly affected by matrix effects. In Sample 1 (see Figures 6a and 6b), both SFI SNMS and SIMS spectra show the presence of cholesterol, C₃₁ diene, and the three wax monoesters. However, in Sample 2, secondary ions are severely suppressed (see Figure 6d), with the cholesterol and wax monoesters signals at the noise threshold. The only high-mass molecules clearly visible in the SIMS spectrum are the C₃₁ triene and the C₃₀H₇₀O₂ wax monoester, with their signal intensities roughly a third of that observed in the SFI SNMS spectra.

The variable degrees of suppression observed in the analytes of Sample 2 are indicative of the complexity of secondary-ion formation in complex biological samples. The combined effects of media and native salts, along with possible ion suppression, are likely responsible for the observed differences between the SIMS and SFI SNMS spectra. In general, since SFI SNMS seems to be much more resistant to matrix ionization effects, it

is hoped that the analytes detected in *B. braunii* could, after proper control experiments, potentially be quantified by future studies. Similar to the cholesterol experiments discussed previously, the severe matrix ionization effects observed in Sample 2 were also present in areas of Sample 1, depending on the probed location.

CONCLUSION

Strong field ionization (SFI) using a powerful ultrafast tunable infrared (IR) laser system can be successfully applied for laser post-ionization secondary neutral mass spectrometry (SNMS) of biological samples. Expanding on the capabilities of established photon absorptive methods, SFI is shown to post-ionize intact extensively σ -bonded molecules with masses in excess of 500 Da, thereby permitting the analyses of biological samples where matrix effects severely suppress the secondary ions detected in standard secondary-ion mass spectroscopy (SIMS) analyses.

Although determination of precise ionization mechanisms is beyond the scope of this work, the extensive fragmentation that is observed in experiments on model patterned films of rubrene suggest that there is a significant nonadiabatic ionization pathway for a fraction of the sputtered molecules. The combined effects of the resulting photodissociation, and the intact post-ionization of pre-existing sputtered fragments, produce low-mass (m/z 1–100) signals that are orders of magnitude higher than the molecular ion. Overall, despite the presence of a degree of photodissociation, in SFI SNMS, the rubrene molecular ion signal was up to five times higher than that in the corresponding SIMS spectra. Considering the limited post-ionization efficiency due to undersampling of the sputtered plume with the laser beam, one finds that this technique can principally enhance the measured signal by at least a factor 20 more than the SIMS signal.

When applied to the analysis of mouse brain tissue sections, SFI SNMS delivers cholesterol molecular ion signals that substantially exceed those observed in SIMS, at certain sampled locations. The suppression of cholesterol secondary ions due to matrix effects from native salts and lipid molecules was likely responsible for its highly variable detection in SIMS. In SFI SNMS, the signal is unaffected by the effects of the local chemical environment, since the post-ionization process is decoupled from the surface and largely determined by the internal energy imparted to the molecule during sputtering and the properties of the laser pulse.

Similar to the brain tissue sections, matrix effects in SIMS analyses of certain *B. braunii* algal samples heavily suppressed the analyte signals. SFI SNMS enabled the detection of cholesterol, C₃₁ diene/triene, and wax monoesters in areas of these samples where the secondary-ion signals were almost nonexistent. The intact post-ionization of these analyte molecules represents the expanded capabilities SFI offers over established photon absorptive methods, which struggle with large extensively σ -bonded molecules.

Although these experiments employed substantial defocusing of the laser to achieve the maximum possible post-ionization efficiency, the resulting beam diameters were still insufficient to overlap with the entire detectable plume of sputtered neutrals. This is particularly important in imaging applications, where the overlap may be influenced by the fact that the primary ion beam is rastered over a relatively large field of view. At present, the extent to which the focus can be expanded while maintaining ionization conditions close to saturation is limited

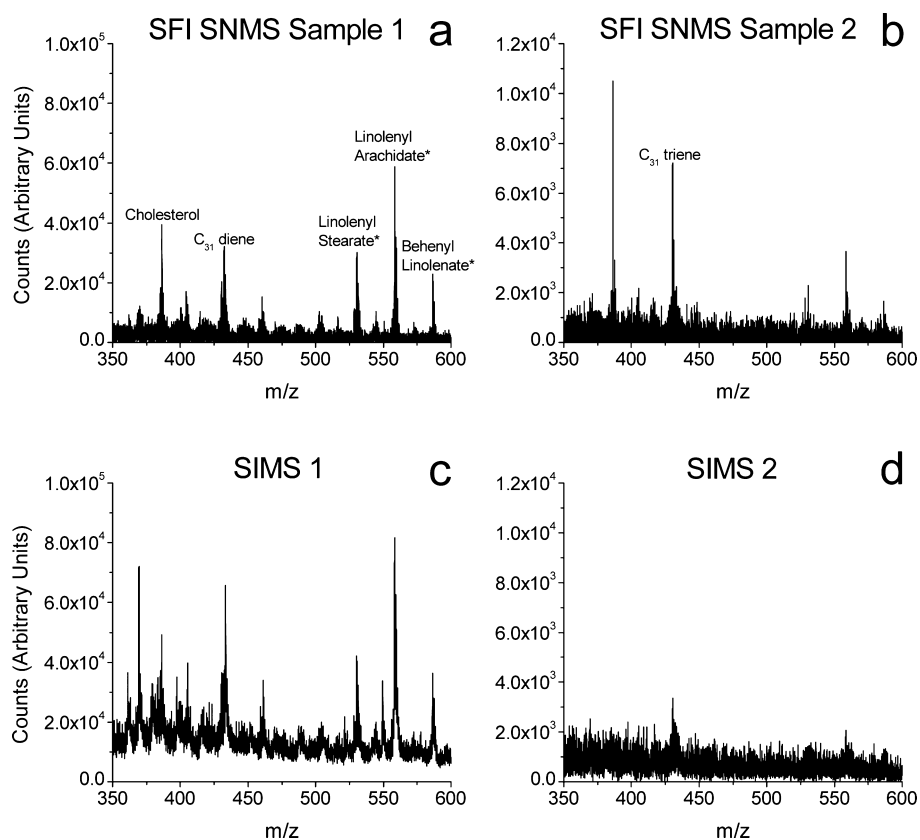


Figure 6. SFI SNMS using 1350 nm, 1.3×10^{13} W/cm² and SIMS mass spectra of two *B. braunii* samples: Sample 1 ((a) SFI SNMS and (b) SIMS) and Sample 2 ((c) SFI SNMS and (d) SIMS).

by the maximum achievable laser power. Therefore, the laser post-ionization (LPI) SNMS signal levels observed in this work may, in principle, be further increased by the introduction of a higher-power laser system, as well as instrumental modifications that involve bringing the laser beam closer to the sample surface without impacting the sample holder stage, and/or configuring the focusing optics for multiple passes through the plume.

The properties exhibited by SFI in the complex biological samples investigated are encouraging to its expanded adoption. Future work may enable quantitative experiments in inhomogeneous biological samples, which are otherwise impossible in SIMS. In addition, combining SFI with the newly developed gas cluster primary ion beams (GCIBs)^{58–60} will allow the use of larger clusters for sputtering. This will provide the dual benefits of decreased sample damage and reduced photodissociation, due to molecules being more softly sputtered, with less internal energy than imparted by smaller clusters. In addition, by overcoming the low secondary-ion yield of large clusters with SFI SNMS, their utility in bioanalysis will further increase.

■ ASSOCIATED CONTENT

📄 Supporting Information

Additional experimental details alluded to in the text, along with Figure S-1 (which shows the chemical structures of the analytes) are available online. This material is available free of charge via the Internet at <http://pubs.acs.org>.

■ AUTHOR INFORMATION

Corresponding Author

*E-mail: nxw@psu.edu.

Notes

The authors declare no competing financial interest.

■ ACKNOWLEDGMENTS

Dr. David Willingham's design and construction of the vapor deposition chamber used in this study is greatly appreciated. Part of this publication was supported by the Pennsylvania State University Materials Research Institute Nanofabrication Lab and the National Science Foundation Cooperative (Agreement No. ECS-0335765). Financial support from the U.S. Department of Energy, Division of Chemical Sciences, Basic Energy Sciences (under Grant No. DE-FG02-06ER15803) is gratefully acknowledged.

■ REFERENCES

- (1) Fletcher, J. S.; Vickerman, J. C.; Winograd, N. *Curr. Opin. Chem. Biol.* **2011**, *15*, 733–740.
- (2) Fletcher, J. S.; Vickerman, J. C. *Anal. Chem.* **2013**, *85*, 610–639.
- (3) Jones, E. A.; Lockyer, N. P.; Kordys, J.; Vickerman, J. C. *J. Am. Soc. Mass Spectrom.* **2007**, *18*, 1559–1567.
- (4) Jones, E. A.; Lockyer, N. P.; Vickerman, J. C. *Int. J. Mass Spectrom.* **2007**, *260*, 146–157.
- (5) Winograd, N.; Baxter, J. P.; Kimock, F. M. *Chem. Phys. Lett.* **1982**, *88*, 581–584.
- (6) Becker, C. H.; Gillen, K. T. *Anal. Chem.* **1984**, *56*, 1671–1674.
- (7) Dyer, M. J.; Jusinski, L. E.; Helm, H.; Becker, C. H. *Appl. Surf. Sci.* **1991**, *52*, 151–157.
- (8) Terhorst, M.; M?llers, R.; Niehuis, E.; Benninghoven, A. *Surf. Interface Anal.* **1992**, *18*, 824–826.
- (9) Winograd, N. *Anal. Chem.* **1993**, *65*, A622–A629.
- (10) Brummel, C. L.; Willey, K. F.; Vickerman, J. C.; Winograd, N. *Int. J. Mass Spectrom. Ion Processes* **1995**, *143*, 257–270.

- (11) Willingham, D.; Kucher, A.; Winograd, N. *Chem. Phys. Lett.* **2009**, *468*, 264–269.
- (12) Veryovkin, I. V.; Calaway, W. F.; Tripa, C. E.; Moore, J. F.; Wucher, A.; Pellin, M. J. *Nucl. Instrum. Methods Phys. Rev., Sect. B* **2005**, *241*, 356–360.
- (13) Veryovkin, I. V.; Calaway, W. F.; Tripa, C. E.; Pellin, M. J. *Nucl. Instrum. Methods Phys. Rev., Sect. B* **2007**, *261*, 508–511.
- (14) Schuhle, U.; Pallix, J. B.; Becker, C. H. *J. Am. Chem. Soc.* **1988**, *110*, 2323–2324.
- (15) Tyler, B. J.; Dambach, S.; Galla, S.; Peterson, R. E.; Arlinghaus, H. F. *Anal. Chem.* **2012**, *84*, 76–82.
- (16) Hrubowchak, D. M.; Ervin, M. H.; Wood, M. C.; Winograd, N. *Anal. Chem.* **1991**, *63*, 1947–1953.
- (17) Willey, K. F.; Brummel, C. L.; Winograd, N. *Chem. Phys. Lett.* **1997**, *267*, 359–364.
- (18) Willey, K. F.; Vorsa, V.; Braun, R. M.; Winograd, N. *Rapid Commun. Mass Spectrom.* **1998**, *12*, 1253–1260.
- (19) Vorsa, V.; Willey, K. F.; Winograd, N. *Anal. Chem.* **1999**, *71*, 574–581.
- (20) Boguslavskiy, A. E.; Mikosch, J.; Gijsbertsen, A.; Spanner, M.; Patchkovskii, S.; Gador, N.; Vrakking, M. J. J.; Stolow, A. *Science* **2012**, *335*, 1336–1340.
- (21) Krausz, F.; Ivanov, M. *Rev. Mod. Phys.* **2009**, *81*, 163–234.
- (22) Willingham, D.; Brenes, D. A.; Wucher, A.; Winograd, N. *J. Phys. Chem. C* **2010**, *114*, 5391–5399.
- (23) Kucher, A.; Winograd, N. *Surf. Interface Anal.* **2013**, *45*, 510–512.
- (24) Levis, R. J.; DeWitt, M. J. *J. Phys. Chem. A* **1999**, *103*, 6493–6507.
- (25) Hankin, S. M.; Villeneuve, D. M.; Corkum, P. B.; Rayner, D. M. *Phys. Rev. Lett.* **2000**, *84*, 5082–5085.
- (26) Hankin, S. M.; Villeneuve, D. M.; Corkum, P. B.; Rayner, D. M. *Phys. Rev. A* **2001**, *64*.
- (27) Lezius, M.; Blanchet, V.; Rayner, D. M.; Villeneuve, D. M.; Stolow, A.; Ivanov, M. Y. *Phys. Rev. Lett.* **2001**, *86*, 51–54.
- (28) Lezius, M.; Blanchet, V.; Ivanov, M. Y.; Stolow, A. *J. Chem. Phys.* **2002**, *117*, 1575–1588.
- (29) Bhardwaj, V. R.; Corkum, P. B.; Rayner, D. M. *Phys. Rev. Lett.* **2003**, *91*.
- (30) Markevitch, A. N.; Smith, S. M.; Romanov, D. A.; Schlegel, H. B.; Ivanov, M. Y.; Levis, R. J. *Phys. Rev. A* **2003**, *68*.
- (31) Markevitch, A. N.; Romanov, D. A.; Smith, S. M.; Schlegel, H. B.; Ivanov, M. Y.; Levis, R. J. *Phys. Rev. A* **2004**, *69*.
- (32) Smith, S. M.; Li, X. S.; Markevitch, A. N.; Romanov, D. A.; Levis, R. J.; Schlegel, H. B. *J. Phys. Chem. A* **2005**, *109*, 10527–10534.
- (33) Smith, S. M.; Li, X. S.; Markevitch, A. N.; Romanov, D. A.; Levis, R. J.; Schlegel, H. B. *J. Phys. Chem. A* **2005**, *109*, 5176–5185.
- (34) Markevitch, A. N.; Romanov, D. A.; Smith, S. M.; Levis, R. J. *Phys. Rev. Lett.* **2006**, *96*.
- (35) Markevitch, A. N.; Romanov, D. A.; Smith, S. M.; Levis, R. J. *Phys. Rev. A* **2007**, *75*.
- (36) Smith, S. M.; Li, X. S.; Markevitch, A.; Romanov, D.; Levis, R. J.; Schlegel, H. B. *J. Phys. Chem. A* **2007**, *111*, 6920–6932.
- (37) Smith, S. M.; Romanov, D. A.; Heck, G.; Schlegel, H. B.; Levis, R. J. *J. Phys. Chem. C* **2010**, *114*, 5645–5651.
- (38) Smith, S. M.; Romanov, D. A.; Li, X. S.; Sonk, J. A.; Schlegel, H. B.; Levis, R. J. *J. Phys. Chem. A* **2010**, *114*, 2576–2587.
- (39) Kotur, M.; Weinacht, T. C.; Zhou, C. Y.; Matsika, S. *Phys. Rev. X* **2011**, *1*.
- (40) Spanner, M.; Patchkovskii, S.; Zhou, C. Y.; Matsika, S.; Kotur, M.; Weinacht, T. C. *Phys. Rev. A* **2012**, *86*.
- (41) Brenes, D. A.; Garrison, B. J.; Winograd, N.; Postawa, Z.; Wucher, A.; Blenkinsopp, P. *J. Phys. Chem. Lett.* **2011**, *2*, 2009–2014.
- (42) Kucher, A.; Wucher, A.; Winograd, N. Submitted to *J. Phys. Chem. C*, **2014**.
- (43) Braun, R. M.; Blenkinsopp, P.; Mullock, S. J.; Corlett, C.; Willey, K. F.; Vickerman, J. C.; Winograd, N. *Rapid Commun. Mass Spectrom.* **1998**, *12*, 1246–1252.
- (44) Weibel, D.; Wong, S.; Lockyer, N.; Blenkinsopp, P.; Hill, R.; Vickerman, J. C. *Anal. Chem.* **2003**, *75*, 1754–1764.
- (45) Wucher, A. In *TOF-SIMS: Materials Analysis by Mass Spectrometry*; Vickerman, J. C., Briggs, D., Eds.; IM Publications and Surface Spectra: Chichester, Manchester, U.K., 2013; pp 217–246.
- (46) Jackson, L. M.; Yoo, J.; Curtis, W.; Winograd, N. To be submitted, **2014**.
- (47) Jackson, L. M.; Yoo, J.; Curtis, W.; Winograd, N. To be submitted, **2014**.
- (48) Garrison, B. J.; Postawa, Z.; Ryan, K. E.; Vickerman, J. C.; Webb, R. P.; Winograd, N. *Anal. Chem.* **2009**, *81*, 2260–2267.
- (49) Valenza, M.; Cattaneo, E. *Prog. Neurobiol.* **2006**, *80*, 165–176.
- (50) McQuaw, C. M.; Zheng, L. L.; Ewing, A. G.; Winograd, N. *Langmuir* **2007**, *23*, 5645–5650.
- (51) Sostarecz, A. G.; Cannon, D. M.; McQuaw, C. M.; Sun, S. X.; Ewing, A. G.; Winograd, N. *Langmuir* **2004**, *20*, 4926–4932.
- (52) Yamaguchi, K.; Nakano, H.; Murakami, M.; Konosu, S.; Nakayama, O.; Kanda, M.; Nakamura, A.; Iwamoto, H. *Agric. Biol. Chem.* **1987**, *51*, 493–498.
- (53) Metzger, P.; Largeau, C. *Appl. Microbiol. Biotechnol.* **2005**, *66*, 486–496.
- (54) Metzger, P.; Berkaloff, C.; Casadevall, E.; Coute, A. *Phytochemistry* **1985**, *24*, 2305–2312.
- (55) Metzger, P.; Allard, B.; Casadevall, E.; Berkaloff, C.; Coute, A. *J. Phycol.* **1990**, *26*, 258–266.
- (56) Georgianna, D. R.; Mayfield, S. P. *Nature* **2012**, *488*, 329–335.
- (57) Largeau, C.; Casadevall, E.; Berkaloff, C.; Dhamelincourt, P. *Phytochemistry* **1980**, *19*, 1043–1051.
- (58) Gnaser, H.; Ichiki, K.; Matsuo, J. *Rapid Commun. Mass Spectrom.* **2012**, *26*, 1–8.
- (59) Rabbani, S.; Barber, A. M.; Fletcher, J. S.; Lockyer, N. P.; Vickerman, J. C. *Anal. Chem.* **2011**, *83*, 3793–3800.
- (60) Wucher, A.; Tian, H.; Winograd, N. *Rapid Commun. Mass Spectrom.* **2014**, *28*, 396–400.